Progress In Electromagnetics Research B, Vol. 82, 115–135, 2018

Design of a Short Range Continuous Wave Compound Phase Coded Linear Frequency Modulation Radar Sensor

Jason Reneau* **and Reza Adhami**

Abstract—The design of a low cost, short range radar sensor based upon a novel phase coded linear frequency waveform is discussed in this paper. The radar sensor utilizes a novel waveform that is produced using digital frequency synthesis techniques. Digital frequency synthesis techniques enable the generation of repeatable, highly linear frequency sweeps and provide a means for accurate application of phase codes to linear frequency modulations. The work presented contains analysis of the component linear frequency and phase code modulations that form the compound phase coded linear frequency modulation. The resulting compound phase coded linear frequency modulation is compared with the component modulations to demonstrate the performance improvement that can be achieved by the combining of radar waveform modulations enabled by modern digital frequency synthesis techniques. The compound phase coded linear frequency modulation waveform shows improved range resolution and suppression of range sidelobes over the individual component waveforms. The phase coded linear frequency modulation shows an improvement of 13 dB over the linear frequency modulation and is only 2 dB less than the phase code. It also achieves a 5 and 10 nanosecond narrower mainlobe autocorrelation peak than the phase code and linear frequency modulation, respectively. A notional signal processing architecture of the waveform is simulated to demonstrate the ability to process the compound waveform. Experimental data collected from a direct digital frequency synthesis based arbitrary waveform generator is compared with the simulated waveform. The compound waveform model and the experimental results show good agreement.

1. INTRODUCTION

Defense, weather monitoring and satellite imaging are typical applications for radar. These applications usually allow for the development of high cost/high complexity solutions for meeting their required sensing performance. The development of low cost, high performance, microwave and electronic integrated circuits (ICs) enables the development of affordable radar sensors for an increasing number of low cost/short range applications including through-wall sensing, automotive collision avoidance, intrusion detection, and autonomous robot navigation [1].

Radar systems can be generally classified as pulsed or continuous wave (CW) systems. A pulsed radar system can make range and velocity measurements of a target using an unmodulated pulsed RF carrier. Coherent pulse trains provide a means to control the range and Doppler resolution [2]. In contrast, an unmodulated CW carrier can only make velocity measurements via the Doppler shift induced by target motion. Additional phase/frequency modulations are applied to both pulsed and CW transmit signals to tailor the range and velocity measurements to achieve the desired radar system performance. The waveform bandwidth and repetition rate/duration of the modulation signal are examples of modulation parameters that are manipulated to meet the specific design goals of a radar system [2, 3].

Received 20 August 2018, Accepted 13 October 2018, Scheduled 22 October 2018
* Corresponding author: Jason Reneau (jmreneau11@msn.com).
The authors are with the Department of Electrical and Computer Engineering, University of Alabama-Huntsville, Huntsville, AL, USA.

The performances of low cost IC devices allow for the synthesis of novel complex wide and ultra-wideband (UWB), radar waveforms [4]. Modern RF synthesis techniques and digital signal processing resources provide radar waveform designers the opportunity for developing increasingly complex waveforms to meet radar system requirements. Examples of these types of waveforms include multi-frequency carrier OFDM [5–7], combined LFM/Barker codes [8, 9] and combined LFM/PRN phase codes [10, 11]. Traditional radar applications for these type of complex waveforms include marine radar [11], synthetic aperture radar (SAR) [12] and collision avoidance radar [13]. Non-traditional applications of these types of complex modulations include ultrasound imaging [14] and combined radar-communication waveforms [7].

Generally, CW radars are used for short range sensing applications due to their low average transmit power and the need for isolation between the transmitter and receiver [15]. Some alternatives to CW systems that are actively being investigated include using portions of communication signals such as IEEE 802.11ad for sensing purposes such as the work described in [16], utilizing frequency modulated interrupted continuous wave (FMICW) to suppress reflections in through wall imaging [17] and multiple-input and multiple output (MIMO) radar [18]. A CW radar architecture was investigated due to its low hardware complexity in order to focus on the development of compound waveforms.

The frequency synthesis and signal processor architectures discussed here are used to produce a compound modulation consisting of linear frequency modulation (LFM) with a bi-phase pseudo random noise code (PRN). The phase coded linear frequency modulation that results from the combination of modulations has desirable properties of both waveforms. The linear frequency modulation is spectrally efficient [19]. The bi-phase code has desirable time side-lobes and provides good pulse compression [20].

The notional frequency synthesis architecture discussed in this paper is intended for implementation using direct digital frequency synthesis (DDFS) techniques. Using DDFS techniques enables the synthesis of highly linear, repeatable frequency ramps. DDFS also provides the control of the phase required to accurately impress the PRN code onto the LFM waveform. The digital nature of the notional frequency synthesis architecture provides a means to change the waveform through software reprogramming rather than hardware modifications, which enables a simplified path to modifying the radar performance. It also provides a means to apply encryption to the waveform on a pulse to pulse or dwell to dwell basis to reduce the ability of a third party to intercept and use the information transmitted by the radar system.

Radar embedded modulation (REM) waveforms have demonstrated desirable performance in terms of covertness in terms of low probability of intercept (LPI) and reliability in terms of symbol error rate (SER) [21, 22] and serve as motivation for the waveform developed in this work. Additionally the combining of techniques such as TR-MUSIC [23], SAR coherent change detection (CCD) method discussed in [24] and polarimetric radar [25] with a compound PCLFM type modulation could provide additional performance benefits.

The organization of the manuscript discussing the development of the continuous wave (CW) radar sensor that transmits a phase coded linear frequency modulated (PCLFM) waveform is as follows. Section 2 contains an overview of the notional radar sensor system, the frequency synthesis and signal processing architecture and background on direct digital frequency synthesis. Section 3 presents the compound PCLFM waveform that results from the combination of component LFM and bi-phase PRN waveforms. The time domain, frequency domain, instantaneous phase and instantaneous frequency behavior of the PCLFM waveform are detailed in Section 4. Section 4 also contains an analysis of the ambiguity function and autocorrelation of the PCLFM waveform. The signal processing architecture of the radar system is developed in Section 5. In Section 6 measurement data of the PCLFM waveform are compared with simulated results. Finally, in Section 7 conclusions on the radar sensor development and novel PCLFM waveform are drawn along with future avenues of investigation.

The notation used in the following text is as follows, $(\cdot)^*$, $\delta(\cdot)$, $|(\cdot)|$ denote conjugation, delta function and norm, respectively j denotes the imaginary unit.

2. RADAR SYSTEM

The design of a low power, continuous wave (CW) phase coded frequency modulated short range radar sensor for detecting and tracking human and vehicle targets is discussed in this paper. S-

band was selected for the system because of the performance, cost and component availability for prototyping. The selected carrier frequency for the system falls within those S-band frequencies allocated for radio navigation by the U.S. Department of Commerce, National Telecommunication and Information Administration, Office of Spectrum Management [26]. The selection of a fan type antenna, with a wide azimuth beamwidth and narrow elevation beamwidth was made compatible with the tracking of pedestrian (human) and vehicle targets. A wide swath of azimuth is desirable so that a single radar sensor can detect targets over a large area, minimizing the number of sensors required.

The system design parameters for the short range radar sensor are given in Table 1.

Table 1. Notional short range radar system parameters.

Parameter	Value
Transmit Power, P_t	250 milli-Watts
Transmit Antenna Gain, G_t	21 dB
Transmit Loss, L_t	1 dB
Receive Antenna Gain, G_r	21 dB
Receive Loss, L_r	1 dB
Antenna Beamwidth, θ_{az},θ_{el}	60°, 3°
Transmit Frequency, f_c	3.250 GHz
Receiver Noise Figure, N_f	8 dB
Signal Processing Loss, L_s	4 dB
Target RCS, σ	0 dBsm (pedestrian), or 10 dBsm (vehicle)

The system parameters in Table 1 are used along with waveform parameters in Table 2 to calculate the expected signal to noise ratio (SNR) versus range using (1). The results of the signal to noise ratio calculations using the time-bandwidth product of the linear frequency modulation as a baseline are plotted in Figure 1, for the vehicle (blue) and pedestrian (red) along with a horizontal black, dashed line that represents a 13 dB threshold for target detection [3]. Figure 1 indicates that the notional sensor should be able to detect a vehicle target at approximately 1200 meters and a pedestrian target at approximately 700 meters.

$$SNR = \frac{P_t G_t G_r \lambda^2 \sigma}{(4\pi)^3 \, kT_o R^4 N_f L B_w} \, (T_s \Delta F) \tag{1}$$

In the expression for the SNR given in Eq. (1), $\lambda = \frac{c}{f_c}$ is the wavelength of the transmit frequency where c is the speed of light in a vacuum, k the Boltzmann constant, T_0 the reference temperature of 290°K, R the slant range between the radar and the target, L the total system loss given by $L = L_t + L_r + L_r$, and B_w the receiver bandwidth. The remaining parameters in the equation are defined in Table 1 and Table 2.

The range resolution of the notional system is given by

$$R_{res} = \frac{c}{2\Delta F} \tag{2}$$

where c is the speed of light, and ΔF is the sweep bandwidth of the linear frequency modulation [3]. In this case the range resolution is 3 meters. The velocity resolution of the system provided by the waveform is given by

$$V_{res} = \frac{\lambda}{2T_s} \tag{3}$$

where λ is the wavelength of the carrier, and T_s represents the sweep time of the linear frequency modulation [3]. The velocity resolution of the notional system was calculated to be approximately 2254 meters per second.

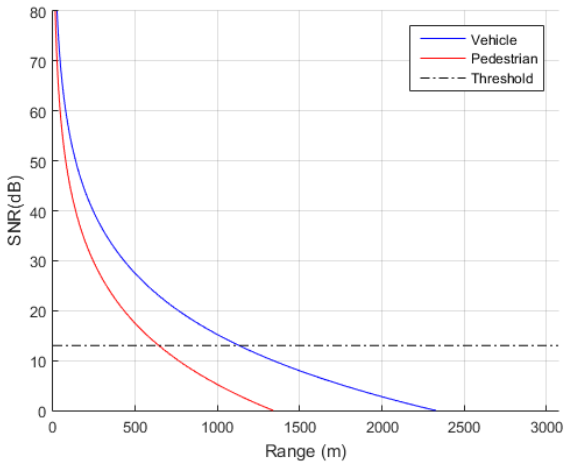

Figure 1. Notional system signal to noise ratio versus range.

Table 2. Waveform modulation parameters.

Linear Frequency Modulation	
Sweep Time, T_s	20.48 microseconds
Sweep Bandwidth, ΔF	50 MHz
Sweep Direction	Up
Phase Code Modulation	
Code Type	Bi-Phase Pseudo Random Noise Code
Number of Chips	1024
Chip Duration (Width)	20 nanoseconds
Chip Frequency	50 MHz

2.1. System Architecture

Figure 2 contains a block diagram of the radar sensor frequency synthesis architecture and signal processor. The sensor consists of two major sections; a digital section and RF section.

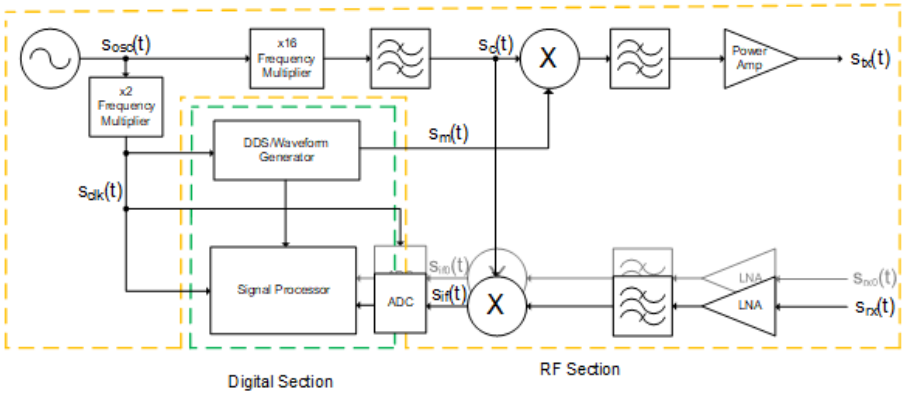

Figure 2. Short range radar sensor frequency synthesis and processing architecture.

The digital section is targeted for implementation using field programmable gate array (FPGA) technology and is responsible for the waveform modulation signal generation and target return signal processing. The use of direct digital frequency synthesis (DDFS) techniques to implement the waveform generator enables the synthesis of complex modulations that consist of both phase and frequency component modulation [27]. These techniques also provide improved frequency sweep linearity, return to the sweep start frequency/phase and the ability to change the phase of the generated modulation signal at each time step [28]. Since the DDFS waveform synthesis is controlled digitally via software and/or firmware, it also provides a means for the reprogramming of the waveform to achieve performance improvements or meet new requirements. The notional waveform generator used to produce the phase coded linear frequency modulation discussed here requires a DDFS module capable of producing a linear frequency ramp based upon the desired start frequency, stop frequency and frequency slope along with a phase control register that provides an additional means to manipulate the phase of the modulation signal, $s_m(t)$.

In addition to the DDFS function of the waveform generator the digital section also processes the target return received by radar sensor. The proposed signal processing architecture contains two parallel receive channels that digitally filter, demodulate and form range/Doppler images from the sampled intermediate frequency (IF) of the target return. The demodulation of the target return is accomplished by multiplying the fast time FFT by the conjugation of the signal modulation and taking the inverse FFT. Once a sufficient number of fast time FFTs have been obtained, the slow time FFT is computed to form a range/Doppler image. The signal processor uses the range/Doppler image to detect targets and make measurements on them. Non-coherent integration of the independent receive channels is used for signal detection. Once targets are detected measurements of velocity, range and angle are made which are passed to higher level processing algorithms that perform target tracking functions. The differential electrical phase between the target measurements in each receive channel is used along with knowledge of the physical antenna spacing to compute the spatial angle to the target using phase interferometry.

The RF frontend is composed of transmit and receive sections. The block diagram of the continuous wave system shown in Figure 2 transmits and receives simultaneously and uses a heterodyne architecture to up convert the modulation to the desired transmit frequency and down convert the target return to an IF for processing. The RF section mixes the modulation signal, $s_m(t)$, generated in the digital section onto the RF carrier signal, $s_c(t)$, that is formed by frequency multiplication of the master oscillator. The resulting output signal of the mixer, $s_{tx}(t)$, is then filtered and amplified.

In each receive channel of the architecture shown in Figure 2 the target return signals ($s_{rx}(t)$ and $s_{rx0}(t)$) are amplified by an low noise amplifier to set the noise figure. The amplified signals are then mixed with the RF carrier to down convert the target returns to IF ($s_{if}(t)$ and $s_{if0}(t)$) for sampling

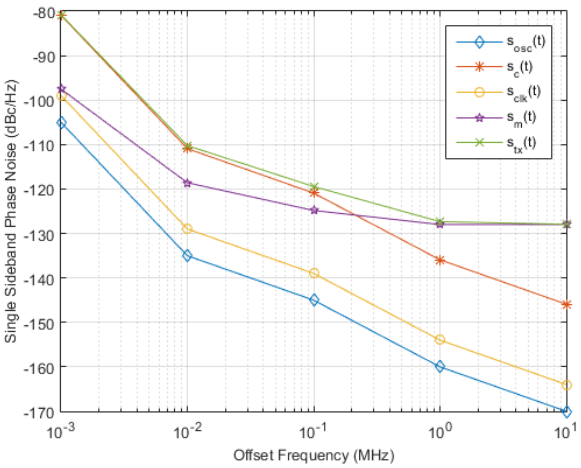

Figure 3. Frequency synthesis architecture signal phase noise.

and processing. The sampled IF signals are provided as inputs into the signal processor.

The expected phase noise of the signals shown in the frequency synthesis architecture of Figure 2 is plotted in Figure 3. Phase noise represents instabilities in the oscillator of a RF sensor. It can be caused by a variety of sources including electronic noise and environmental effects such as vibration [29]. The phase noise propagated through the frequency synthesis architecture serves to raise the noise floor and limits the detection of small targets returns in the close vicinity of large target returns [30]. Figure 3 was generated by propagating the phase noise of the oscillator through the frequency synthesis architecture in Figure 2. The multipliers increase the phase noise of the oscillator by a factor of $20\log_{10}(N)$ where N is the multiplication factor, and the resulting phase noise is further increased by the active components in the RF chain.

2.2. Direct Digital Frequency Synthesis

A classic architecture for the digital synthesis of analog waveforms was proposed by Tierney et al. [31]. A simplified block diagram of a pulsed type direct digital frequency synthesizer (DDFS) based on the classic architecture is shown in Figure 4 [32]. The conventional architecture shown in Figure 4 forms the basis for many modern DDFS devices and is used as the basis for the analysis discussed in this paper.

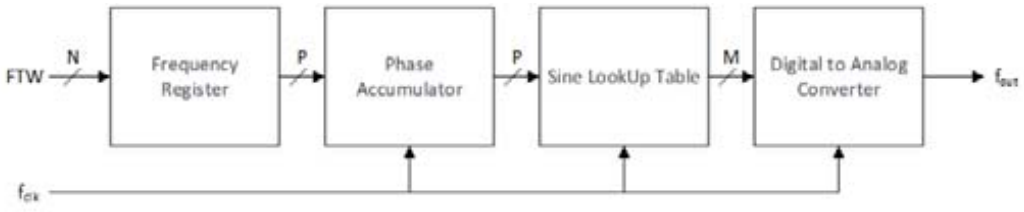

Figure 4. DDFS block diagram.

In the block diagram shown in Figure 4, an N bit frequency tuning word (FTW) is applied to a frequency register. The frequency tuning word was calculated using the expression:

$$FTW = round\left(\frac{f_{desired}}{f_{clock}}2^N\right), \tag{4}$$

where $f_{desired}$ is the desired output DDFS frequency, f_{clock} the frequency used to clock the DDFS, and N the number of bits in the frequency accumulator [33]. The actual output frequency from the DDFS is calculated using:

$$f_{output} = \frac{FTW\, f_{clock}}{2^N}. \tag{5}$$

In this expression f_{output} is the output frequency from the DDFS. The phase accumulator is clocked and accumulates a value that represents the phase angle increment. A register containing phase offset word (POW) is used to allow the manipulation of the phase accumulator. The expression is for calculating the POW given in Eq. (6). The phase offset word can be used to apply an arbitrary phase or start the phase at a desired state. P bits of the phase angle increment are used to index the sine look up table (LUT) at each clock cycle. In the example discussed there the number of bits in the phase accumulator (P) and the frequency tuning word (N) are equal; in many DDFS implementations this is not the case, and additional quantization occurs in the form of phase truncation that introduces undesired spurious frequency content into the DDFS output spectrum [32, 33]. The M bits output from the sine (LUT) is applied to a digital to analog converter that converts the digital input to the desired analog frequency output.

$$POW = round\left(\frac{\Delta\theta}{360}2^P\right) \tag{6}$$

The classical pulse type DDFS architecture shown in Figure 4 produces a single output frequency specified by the frequency tuning word. The digital structure of the DDFS allows the manipulation of

the digital structures (registers, accumulators, etc.) to apply complex modulation of the output DDFS frequency including phase, frequency and amplitude modulations [32]. Applying modulation digitally to the DDFS output provides a means to repeatedly generate wide bandwidth, fine frequency resolution and low phase noise waveforms [34]. DDFS provides high precision and resolution enabling highly linear frequency chirps [35]. Table 3 contains DDFS module parameters suitable for generating the PCLFM waveform discussed in the following sections.

Table 3. DDFS module parameters.

f_{clock}	1200 MHz
Phase Accumulator (N)	32 Bits
Phase Offset Register (P)	16 Bits
Digital To Analog Converter (M)	14 Bits

3. COMPOUND WAVEFORM DEVELOPMENT

DDFS technology enables the generation of complex waveforms that consist of a combination of modulations commonly used by radar systems. The phase coded linear frequency modulation (PCLFM) compound waveform examined in this work consists of a phase coded waveform combined with a linear frequency modulation. The combination is used to obtain a waveform that provides desirable properties of both waveform types.

The transmit waveform is composed of two components, a radio frequency (RF) carrier and modulation. The equation for the transmitted signal is given by

$$s_{tx}(t) = s_c(t)\, s_{mod}(t), \tag{7}$$

where $s_c(t)$ is the carrier signal, and $s_{mod}(t)$ is the modulation signal. The carrier signal is represented by the complex exponential,

$$s_c(t) = e^{j2\pi f_c t}, \tag{8}$$

where f_c is the frequency of the RF carrier. The modulation signal $s_{mod}(t)$ is composed of two modulation signals, a linear frequency modulation component, $s_{lfm}(t)$, and a phase code modulation component, $s_{pc}(t)$. The equation for the modulation signal is given by

$$s_{mod}(t) = s_{lfm}(t)\, s_{pc}(t). \tag{9}$$

The following sub sections examine the component modulations and the resulting compound modulation.

3.1. Linear Frequency Modulation Signal

The linear frequency modulation component of Eq. (9), $s_{lfm}(t)$, is expressed in complex exponential form as:

$$s_{lfm}(t) = e^{j\left(\phi_{lfm}(t)\right)}, \tag{10}$$

where the phase, $\phi_{lfm}(t)$, is related to the instantaneous frequency by [15]

$$\phi_{lfm}(t) = 2\pi \int_0^t f_{lfm}(\tau)\, d\tau. \tag{11}$$

The instantaneous frequency $f_{lfm}(t)$ is given by [15]

$$f_{lfm}(t) = \frac{\Delta F}{T_s} t, \tag{12}$$

where ΔF is the sweep bandwidth, and T_s is the sweep duration of the modulation. The slope of the linear frequency ramp is given by $\frac{\Delta F}{T_s}$. Substituting Eq. (12) into Eq. (11) and performing the

integration results in an expression of the phase in terms of the sweep bandwidth and sweep duration as a function of time,

$$\phi_{lfm}(t) = \pi \frac{\Delta F}{T_s} t^2. \tag{13}$$

3.2. Phase Code Modulation Signal

The second component of the modulation signal in Eq. (9) is the phase code modulation which is given by

$$s_{pc}(t) = e^{j(\phi_{pc}(t))}. \tag{14}$$

The expression for the phase code modulation, $\phi_{pc}(t)$, is found by summing the individual phase code elements or chips at each instant in time [36]

$$\phi_{pc}(t) = \sum\nolimits_{i=0}^{M-1} \phi_{code_i} rect\left(\frac{t - i\tau_c}{\tau_c}\right). \tag{15}$$

where M represents the number of chips in the phase code, ϕ_{code} the ith chip in the phase code, and τ_c the chip duration. The rect function is used to define the chip over the total duration of the phase code:

$$rect(x) = \begin{cases} 1, & 0 \le x \le 1 \\ 0, & elsewhere \end{cases}, \quad 0 \le x < T_s. \tag{16}$$

The duration of each phase code chips is given by

$$\tau_c = \frac{T_s}{M}, \tag{17}$$

with T_s being the total duration of the phase code sequence.

3.3. Compound Phase Coded Linear Frequency Modulation Signal

The compound waveform is given in Eq. (9), and substituting the complex exponential forms of the linear frequency modulation and phase code modulation gives

$$s_{mod}(t) = e^{j\left(\phi_{lfm}(t)\right)} e^{j(\phi_{pc}(t))}. \tag{18}$$

Using the rules of exponential functions and factoring this can be rewritten as

$$s_{mod}(t) = e^{j\left(\phi_{lfm}(t) + \phi_{pc}(t)\right)}. \tag{19}$$

The phase of the compound modulation is

$$\phi_{mod}(t) = \phi_{lfm}(t) + \phi_{pc}(t). \tag{20}$$

Substituting the expressions for the phase of the linear frequency modulation in Eqs. (13) and (15) results in the expression

$$\phi_{mod}(t) = \pi \frac{\Delta F}{T_s} t^2 + \sum\nolimits_{i=0}^{M-1} \phi_{code_i} rect\left(\frac{t - i\tau_c}{\tau_c}\right). \tag{21}$$

The instantaneous frequency of the modulation can be obtained using the relationship given in Eq. (11). To obtain an expression for the instantaneous frequency the derivative of the phase is taken.

$$\frac{d}{dt}\left[\phi_{mod}(t)\right] = \frac{d}{dt}\left[\pi \frac{\Delta F}{T_s} t^2 + \sum\nolimits_{i=0}^{M-1} \phi_{code_i} rect\left(\frac{t - i\tau_c}{\tau_c}\right)\right]. \tag{22}$$

Breaking up this expression using the rules of differentiation gives:

$$\frac{d}{dt}\left[\phi_{mod}(t)\right] = \frac{d}{dt}\left[\pi \frac{\Delta F}{T_s} t^2\right] + \frac{d}{dt}\left[\sum\nolimits_{i=0}^{M-1} \phi_{code_i} rect\left(\frac{t - i\tau_c}{\tau_c}\right)\right]. \tag{23}$$

Carrying out the differentiation of the individual terms results in the expression:

$$\frac{d}{dt}\left[\phi_{mod}\left(t\right)\right] = 2\pi\frac{\Delta F}{T_s}t + \left[\frac{1}{\tau_c}\sum\nolimits_{i=0}^{M-1}\phi_{code_i}\delta\left(\frac{t-i\tau_c}{\tau_c}\right)\right]. \tag{24}$$

where we have used the chain rule along with the knowledge that derivative of the rectangle function, when taken results in an impulse function ($\delta(t)$), to carry out the derivative operation on the second term of Eq. (23). Using the relationship between instantaneous phase and frequency given in Eq. (11) solved to obtain the instantaneous frequency gives:

$$f_{mod}\left(t\right) = \frac{1}{2\pi}\frac{d}{dt}\left[\phi_{mod}\left(t\right)\right]. \tag{25}$$

Substituting the expression for the derivative of the phase, Eq. (24), into the expression for the instantaneous frequency, Eq. (25), results in

$$f_{mod}\left(t\right) = \frac{\Delta F}{T_s}t + \frac{1}{2\pi\tau_c}\sum\nolimits_{i=0}^{M-1}\phi_{code_i}\left(\delta\left(\frac{t-i\tau_c}{\tau_c}\right)\right). \tag{26}$$

The equation for the instantaneous frequency of the PCLFM found is given in Eq. (26). The first term in Eq. (26) has the form of a linear ramp, while the second term is a series of impulses that occur at the chip boundaries.

The expression for the PCLFM is given by Eq. (27). It is found by substituting the phase component of the linear frequency modulation in Eq. (13) and bi-phase code modulation in Eq. (15) into Eq. (19).

$$s_{mod}\left(t\right) = e^{j\left(\pi\frac{\Delta F}{T_s}t^2 + \sum\limits_{i=0}^{M-1}\phi_{code_i}rect\left(\frac{t-i\tau_c}{\tau_c}\right)\right)}. \tag{27}$$

4. COMPOUND WAVEFORM ANALYSIS

The expression given in Eq. (27) was used along with the waveform parameters in Table 2 to generate the time domain, frequency domain, instantaneous phase, instantaneous frequency, ambiguity function and autocorrelation plots shown in the sub-sections that follow. The waveform parameters given in Table 2 were chosen to provide the performance necessary for a short range continuous wave radar sensor.

While any bi-phase code sequence will introduce discontinuities into the modulation necessary to spread the frequency, a pseudo random noise bi-phase code was chosen because of its autocorrelation properties and the ability to generate codes of a specified length using a linear feedback shift register

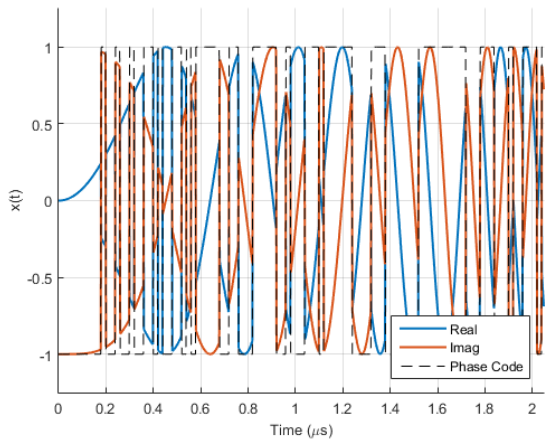

Figure 5. Time Domain representation of phase coded linear frequency modulation.

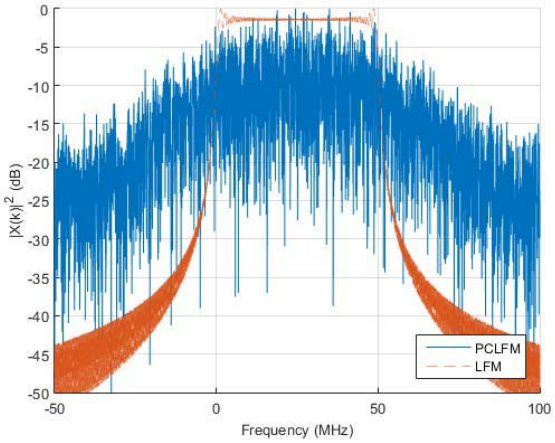

Figure 6. Frequency domain representation of phase coded linear frequency modulation.

(LFSR) technique [3]. A randomly generated phase code was used to develop the compound PCLFM. The length of the phase code was chosen in order to match the chip bandwidth, $\frac{1}{\tau_c}$ to the sweep bandwidth of the linear frequency modulation, T_s.

4.1. Time Domain

Figure 5 contains the time domain plot of the real (blue) and imaginary (red) components of the PCLFM waveform. The phase code imposed on the modulation is also shown as a black dashed line in the figure. Only one-tenth of the sweep time, T_s, is shown so that the phase transitions can be observed. The phase discontinuities introduced into the linear frequency ramp by the phase code are clearly observable in Figure 5.

4.2. Frequency Domain

In Figure 6 the frequency domain representations of the PCLFM signal (blue) and LFM (red) are plotted together in order to illustrate the frequency spreading effect introduced by the phase code. The combination of the PRN with the LFM has completely obscured the spectrum of the component modulations. The PCLFM has taken on a noise like quality.

4.3. Instantaneous Phase

Figure 7 contains plots of the unwrapped instantaneous phases of the PCLFM (red) and LFM (blue). Both have the exponential shape characteristic of an increasing linear frequency ramp modulation. Although it cannot be easily observed in Figure 7(a) due to the scale of the axes the phase of the PCLFM modulation contains phase jumps of $\pm\frac{\pi}{2}$. The axes of Figure 7(b) have been adjusted to show one-tenth of the PCLFM sweep. The discontinuities in the instantaneous phase of the PCLFM are readily apparent. The PRN code sequence serves to introduce positive and negative going discontinuities.

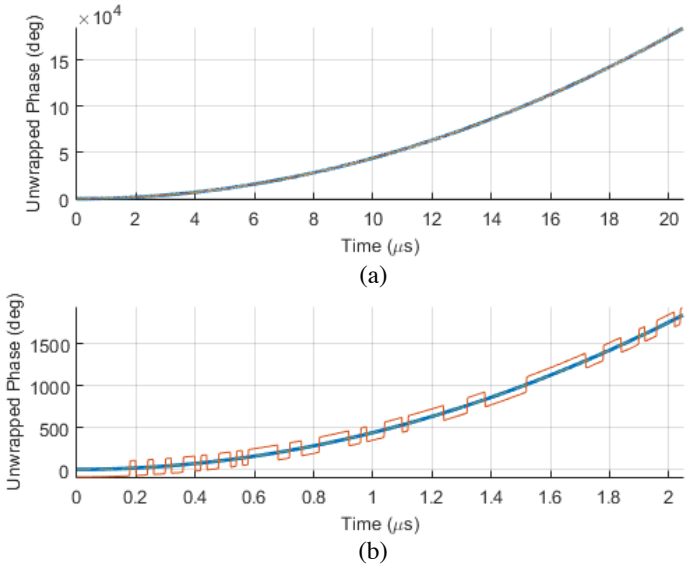

Figure 7. Instantaneous phase of phase coded linear frequency modulation.

4.4. Instantaneous Frequency

The instantaneous frequency is shown in Figure 8. The instantaneous frequency associated with the LFM (blue) is plotted along with the PCLFM (red). The blue trace of the LFM linearly increases from the starting frequency (0 Hz) to the stop frequency (50 MHz). The PCLFM shows the same linear

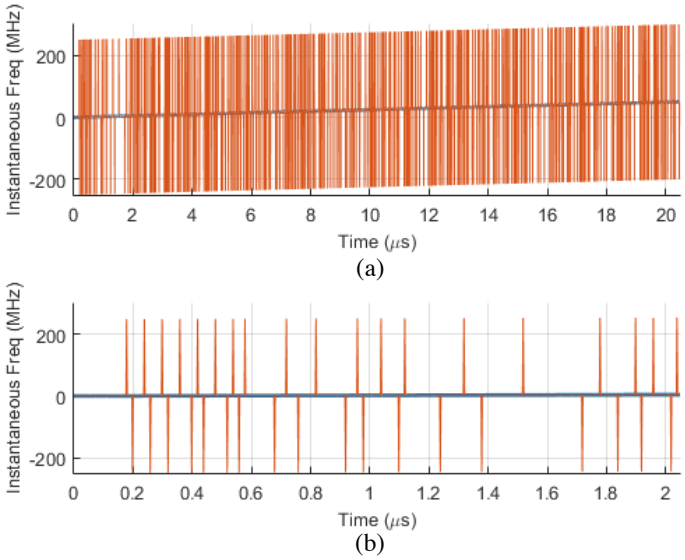

Figure 8. Instantaneous frequency of phase coded linear frequency modulation.

ramp along with frequency jumps of ±250 MHz. The magnitude of the discontinuities are related to the sampling rate of the waveform. The model of the PCLFM modulation calculates the instantaneous frequency, $f_{mod}(n)$, using estimates of the derivative of the instantaneous phase, θ using the difference between adjacent values divided by the sampling interval, t_s

$$f_{mod}\left(n\right) = \frac{1}{2\pi}\left[\frac{\theta_n - \theta_{n-1}}{t_s}\right]. \tag{28}$$

A sampling interval of 2 ns, corresponding to a sampling frequency of 500 MHz, was used. Since a bi-phase PRN code is used a difference of π occurs at the chip boundary. Substituting the values into Eq. (28) and solving results in a predicted frequency discontinuity of 250 MHz, which corresponds to the peak values observed in the plot of Figure 8.

4.5. Ambiguity Function

The ambiguity function was computed for the compound modulation to gain insight into the behavior of the modulation. The ambiguity function provides useful characteristics of the waveform behavior including range-Doppler coupling, side lobe structure, and ambiguities [37].

The ambiguity function for a radar waveform with Doppler frequency, f, and time delay, τ, is calculated using

$$\left|\chi(\tau, f)\right|^2 = \left|\int_{-\infty}^{\infty} x\left(t\right) x^*\left(t-\tau\right) * e^{j2\pi ft} dt\right|^2. \tag{29}$$

A technique using the FFT to calculate the ambiguity function described in [36, 38] was used to generate the ambiguity function surface for the PCLFM modulation shown in Figure 9.

The Doppler and delay axes of Figure 9 were normalized by the frequency sweep bandwidth and sweep duration. The plot of the PCLFM ambiguity surface contains the 'thumbtack' like response typical of a phase coded waveform. The 'pyramidal' sloped surface characteristic of a linear frequency waveform has been suppressed by the phase code in the ambiguity surface. The area under the ambiguity function is constant. The expected behavior is that as the mainlobe is narrowed or sidelobes suppressed in one area sidelobes grow as the area is redistributed. In narrowing the peak and suppressing the close in sidelobe level of the LFM by the PRN code, the mean sidelobe level of the PCLFM is raised to a level similar to that of the PRN code.

Figure 10 contains the matched Doppler range cut (a) and matched range Doppler cut (b) of the ambiguity function shown in Figure 9 for the PCLFM (red) along with the LFM (blue) and PRN code (green) generated using the waveform parameters given in Table 2. The matched Doppler range cut of Figure 10(a) shows that the peak width of the phase coded linear frequency waveform (red) has been narrowed more than either of the component modulations (blue and green). Figure 10(a) also shows that the close-in time (range) sidelobes of the linear frequency modulation are suppressed. The plot of the matched range Doppler cut in Figure 10(b) shows that the PCLFM performance is the same as the component modulations.

Table 4 contains data that compare the peak sidelobe level and mainlobe width of the PCLFM, LFM and PRN modulations. The peak sidelobe level (PSL) and mainlobe width are indicators of the ability to detect closely spaced targets and range resolution. In the table the larger the number is, the greater the improvement is. The PCLFM provides a significant improvement in PSL over the LFM and is only slightly behind that of the PRN. The mainlobe width of the PCLFM is narrower than both the LFM and PRN modulations. These results demonstrate that the compound PCLFM provides improved performance over a single modulation type.

Table 4. Waveform improvement comparison.

	Peak to Sidelobe Ratio			Main Lobe Width		
	dB	Improvement		ns	Improvement	
		vs LFM	vs PRN		vs LFM	vs PRN
LFM	−13.3	0	−14.86	24.14	0	−4.16
PRN	−28.16	14.86	0	19.98	4.16	0
PCLFM	−26.2	12.9	−1.96	14.63	9.51	5.35

4.6. Signal Autocorrelation

The autocorrelation of the PCLFM modulation is shown in Figure 11. The PSL of −26 dBc is observed in the autocorrelation plot of the signal in Figure 11(a). The suppression of the close in range sidelobes and narrow mainlobe peak can be observed in the region of the autocorrelation plot shown in Figure 11(b).

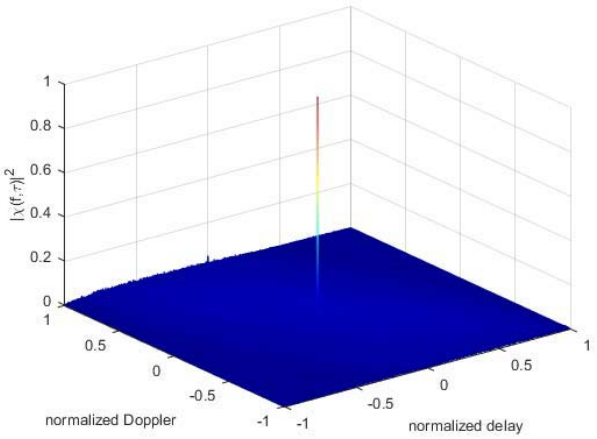

Figure 9. Ambiguity function surface for phase coded linear frequency modulation.

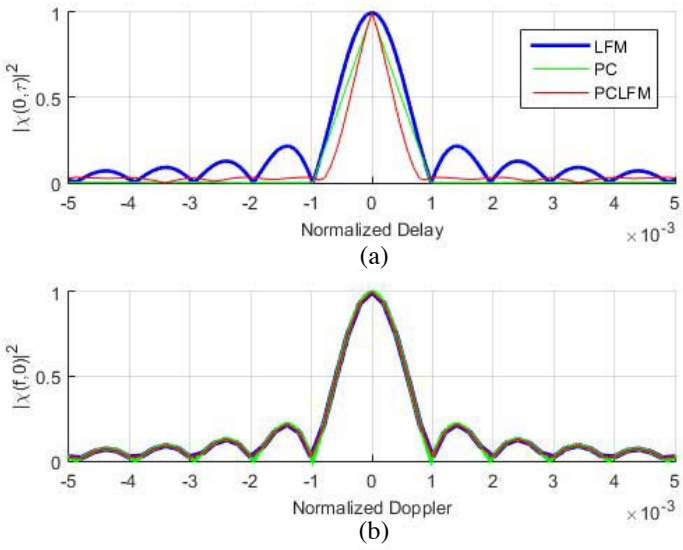

Figure 10. Ambiguity function cuts. (a) Matched doppler range cut. (b) Matched range doppler cut.

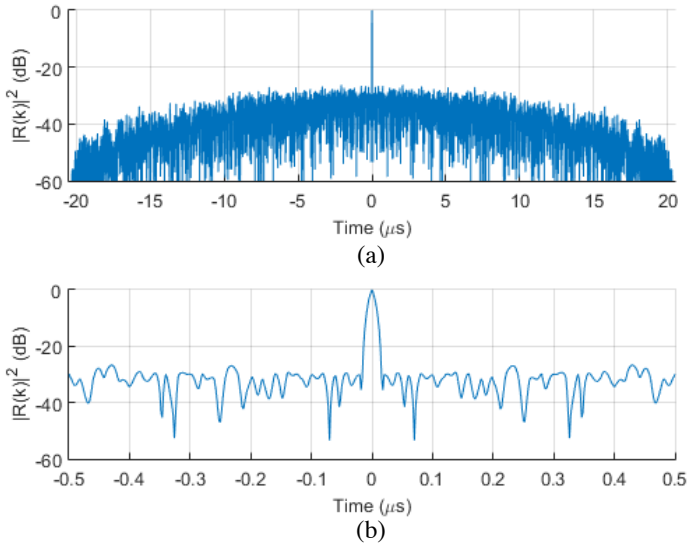

Figure 11. Phase coded linear frequency modulation. (a) Entire autocorrelation. (b) Autocorrelation peak region.

5. SIGNAL PROCESSING

The system architecture and compound phase coded linear frequency modulated waveform discussed in the previous sections was modeled to evaluate the system behavior. The transmitted phase coded linear frequency modulation was simulated, and target returns were modeled for three targets, summarized in Table 5. Two-dimensional FFT processing is used to process the target return [15, 39, 40]. A signal processing block diagram is shown in Figure 12. The signal processing flow shown in the white blocks is implemented for each receive channel. The gray block of Figure 12 performs the processing to extract peaks from the slow time FFT data from each channel to obtain the target range, velocity and angle measurements.

The target return IF signal processing is performed by an FFT based matched filter [36]. In this

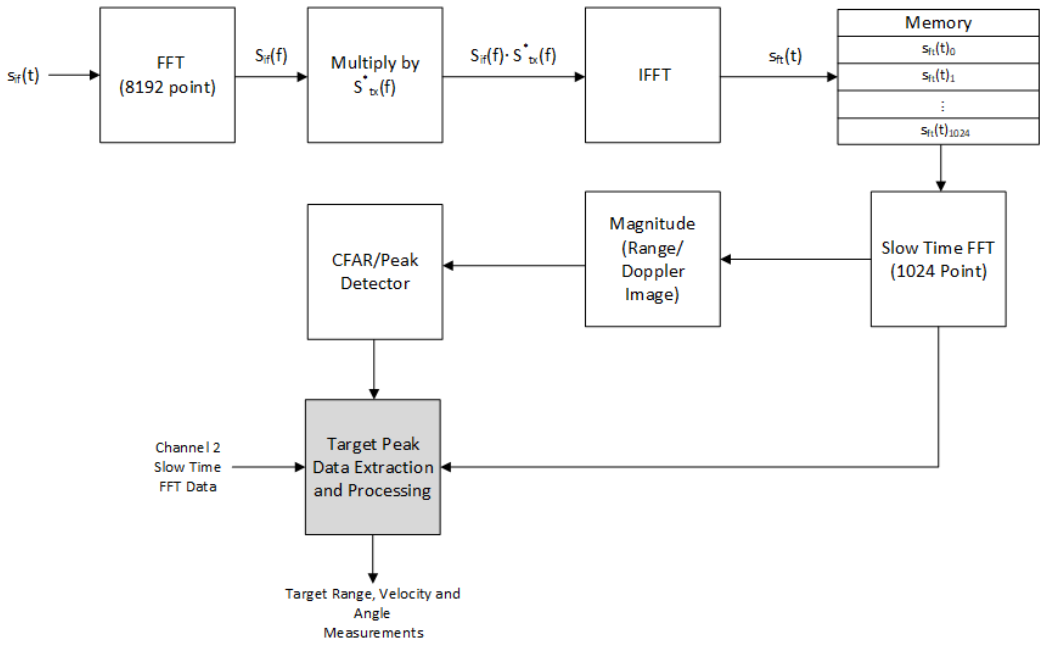

Figure 12. Signal processing block diagram.

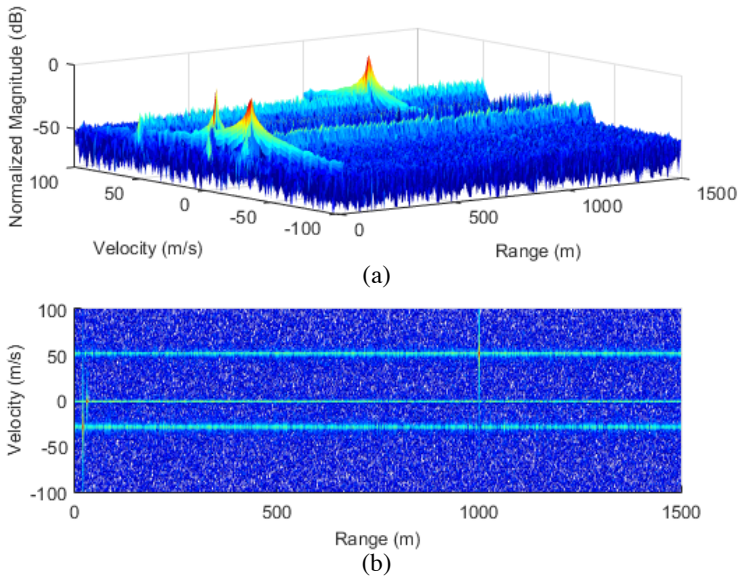

Figure 13. Range doppler map for phase coded linear frequency modulation. (a) 3D view. (b) 2D view.

type of match filter the sampled target return signal is multiplied by a stored copy of the conjugated FFT of the transmit signal and then the inverse FFT taken. The expression for the FFT based matched filter is

$$s_{ft}(t) = IFFT\left[S_{if}(f)\, S^{*}_{tx}(f)\right] \tag{30}$$

where $s_{ft}(t)$ is the fast time matched filter response, $S_{if}(f)$ the FFT of the sampled target return IF signal, and $S^{*}_{tx}(f)$ a stored copy of the conjugated FFT of transmit waveform. The fast time matched filter response provides range information about the target return. Once a set of fast time responses have been collected and stored in memory, another FFT is computed down the rows to obtain velocity

Table 5. Results of signal processing test targets.

	Truth			Measured			Error		
Tgt ID	Range (m)	Velocity (m/s)	Angle (deg)	Range (m)	Velocity (m/s)	Angle (deg)	Range (%)	Velocity (%)	Angle (%)
1	20	−30	1	19.88	−30.81	0.94	−0.63	2.70	−6.02
2	30	−2	10	30.00	−2.20	10.00	0.00	10.04	0.06
3	1000	50	30	999.75	50.62	29.99	−0.03	1.24	0.00

information and form a range/Doppler image. A constant false alarm rate (CFAR) detector is used to detect target using the magnitude of the range/Doppler image. The I and Q data of the peaks identified by the CFAR detector in the range/Doppler image are extracted from each channel and processed into target range, velocity and angle measurements.

An FFT of 8192 points was used to process the fast time (range) response of each sweep, followed by a 1024 point FFT down all of the range bins to obtain the Doppler information shown in Figure 13. The figure corresponds to the box labeled magnitude of Figure 12. The range/Doppler image contains three targets which can be clearly seen in the 3d plot of Figure 13(a) and 2d plot of Figure 13(b). The Doppler axis of Figure 13 has been converted to velocity for clarity. The range, velocity and angle of the targets are provided in Table 5.

The detected peaks associated with the targets are easily identifiable in both plots of Figure 14. The target range is plotted in Figure 14(a). Figure 14(b) contains the Doppler peaks, which have been plotted as velocity for clarity. The red diamonds, shown on the plot, indicate the detected target peaks. A simple peak detection algorithm was used to detect the presence of potential range and Doppler targets based upon a 13 dB threshold. The range data in Figure 14(a) show very narrow peaks expected from the analysis of the PCLFM waveform. After identifying potential range and velocity targets the complex I and Q data of three targets are extracted from the slow time FFT data of each channel and used to compute range, velocity and angle measurements.

Table 5 contains the target parameters (Measured) extracted from the range Doppler image for each of the three target peaks along with the target parameters used as input (Truth) to the signal processing model. The errors between the target input parameters and measured target parameters are calculated and summarized in Table 5.

The errors calculated for range, velocity and angle, summarized in Table 5 indicate that a short range radar system based upon a phase coded linear frequency modulation waveform is capable of making accurate target measurements. The range measurement shows the best agreement with the input (Truth) as evidenced by it having the lowest percent error of the three target parameters. Adding a bin splitting technique to the processing could improves the measurements of range and velocity. The averaging of several target measurements could be used in an actual system to improve the measurement accuracy of the target parameters.

5.1. Probability of Detection and Receiver Operating Characteristic

The probability of detection (P_d) and receiver operating characteristic were examined for the notional radar system. The single sweep probability of detection curves is given in Figure 15 for Swerling targets [41], where a Swerling 0 or 5 target represents a constant RCS model; Swerling 1 and 2 targets are represented using a chi-squared density function with two degrees of freedom; Swerling 3 and 4 targets are represented with a chi-squared density function with four degrees of freedom [36]. A probability of false alarm of $1.1921 \cdot 10^{-7}$ was calculated from the total number of range/Doppler cells formed in the signal processor. Using a 13 dB threshold, (black dashed line) predicts that a Swerling 0 and 5 target has an 80 percent probability of detection, that a Swerling 3 and 4 target has a 55 percent probability of detection and that Swerling 1 and 2 target has a 47 percent probability of detection.

The receiver operating characteristic (ROC) curve is shown in Figure 16. A signal to noise ratio of

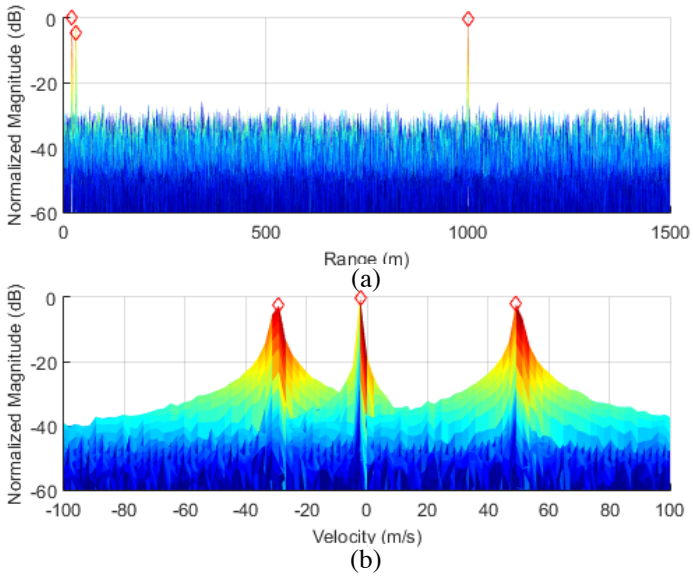

Figure 14. Phase coded linear frequency modulation signal processing. (a) Column sum and (b) row sum.

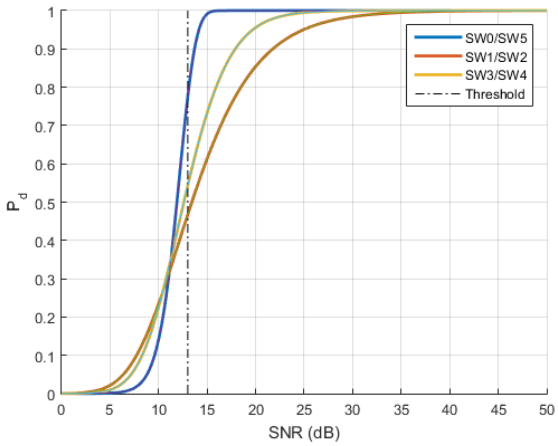

Figure 15. Probability of detection curve.

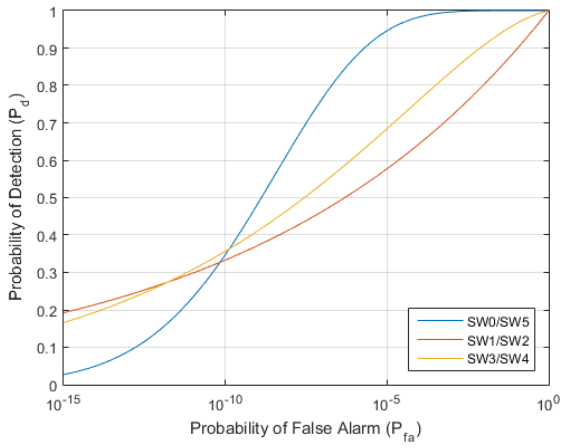

Figure 16. Receiver operating curve for a target SNR of 13 dB.

13 dB was used to generate the plot of the ROC for Swerling 0 and 5, Swerling 1 and 2 and Swerling 3 and 4 targets.

6. EXPERIMENTAL RESULTS

6.1. Phase Coded Linear Frequency Modulation Synthesis

The signal processing model used to generate the plots shown in the previous section was used to generate a waveform file that was downloaded to a Tektronix 5404 arbitrary waveform generator (AWG) in order to verify that the waveform could be generated in hardware. The synthesized PCLFM waveform output by the AWG was captured using a high-speed digital oscilloscope (Tektronix MSO4104B) sampling at 5 Gsps.

The frequency spectrum of the measured (blue) and expected (red) is shown in Figure 17. The

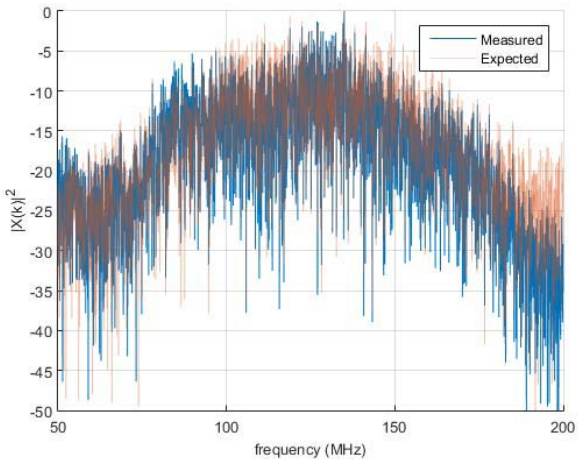

Figure 17. Frequency domain plot of experimentally generated phase coded linear frequency modulation.

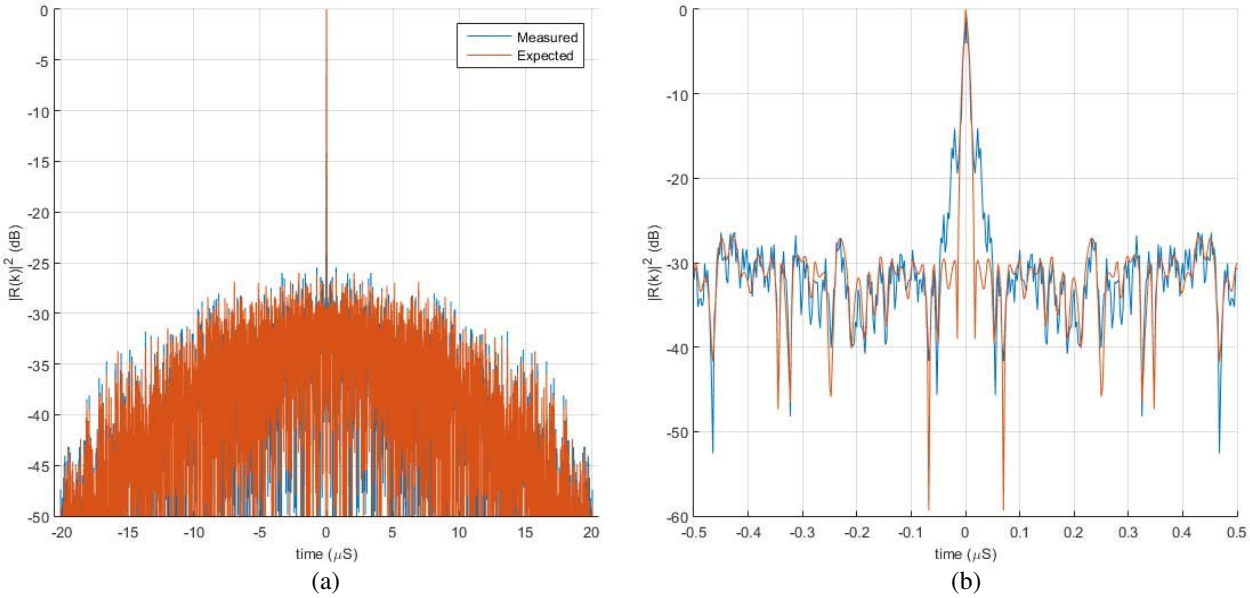

Figure 18. Experimentally generated phase coded linear frequency modulation. (a) Entire autocorrelation. (b) Autocorrelation peak region.

collected data were resampled at 400 MHz to match the sampling rate of the notional system. The frequency spectrum was computed by taking an 8192 point FFT of the down sampled waveform data. The spectra of the hardware generated waveform demonstrates a high degree of similarity with the expected waveform shown in the figure. The difference between the magnitudes of the measured and expected data shown in Figure 17 is attributed to the experimental test setup. There was no analog filtering present to prevent high frequency noise from aliasing into the data collection. The rolloff of the AWG also played a role in the spectral shape of the measured data. These test setup errors also impact the autocorrelation plots computed using the measurement data shown in Figure 18.

The results of the computation of the autocorrelation for the measured digitally synthesized and down sampled (blue) and expected (red) PCLFM waveform data are shown in Figure 18. Figure 18(a) shows the entire autocorrelation of the waveform while Figure 18(b) contains a zoomed in region about

the autocorrelation peak. The autocorrelation of the experimentally obtained PCLFM waveform shows good agreement with the simulation. In both signals the nulls of the main lobe occur at approximately $\pm 0.016\,\mu s$. The sidelobe level of the measured and expected waveforms is approximately the same. The location of the nulls in the sidelobes also occur at the same time/range in both data sets plotted in Figure 18.

6.2. Phase Coded Linear Frequency Modulation Waveform Processing

A target return at 1000 meters was created by time shifting (delaying) the measured PCLFM signal. The target return was then processed using the first three steps for processing the fast time FFT shown in Figure 12. An 8182 point FFT was taken of the sampled PCLFM waveform, then multiplied by the conjugated FFT of the ideal PCLFM modulation, followed by taking the inverse FFT of the complex product to obtain the range (time delay) to a target. The result of this processing is shown in Figure 19 for both the measured signal (blue) and ideal signal (red).

The plots of Figure 19 show the magnitude of the return versus the time delay in (a) and the magnitude versus range in (b). The red dots indicate peaks that would be detected using a threshold of 13 dB signal to noise ratio. In this case there should be only a single peak located at 1000 meters. The second peak that occurs at approximately -14 dBc and at a range of approximately 996 meters is introduced by the high frequency noise content present in the measured signal. The measured signal has the narrow peak and noise floor at -30 dBc observed in the autocorrelation of the expected signal. Improving the experimental setup using filtering would improve performance and eliminate the undesired peak.

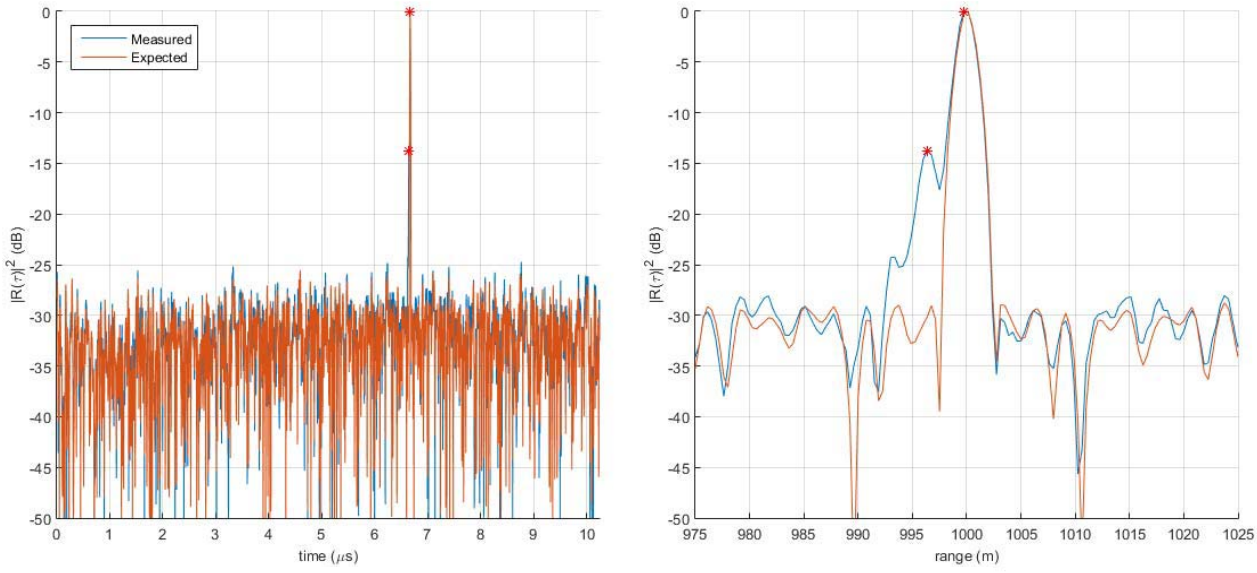

Figure 19. DDFS generated phase coded linear frequency modulation cross correlation using FFT.

7. CONCLUSIONS

The design of a short range radar system and analysis of a PCLFM consisting of a bi-phase PRN code and LFM was presented. The mathematical basis of the compound waveform was discussed and simulated results presented. The analysis of the waveform demonstrates that the proposed compound modulation can provide a narrowed mainlobe peak, improved time sidelobe suppression and frequency spreading. The narrowing of the autocorrelation peak yields greater range resolution. The suppressing of the sidelobes adds improved ability to resolve closely spaced targets, and the frequency spreading

gives improved interference performance and makes the intercept of the transmitted waveform less likely. Combining the LFM and the PRN code imparts an increase in the bandwidth of the modulation leading to the improvement in the waveform performance.

An experimental hardware setup was used to digitally synthesize and capture the PCLFM waveform. The results of the data collection verify the performance of the results obtained from the simulated waveform demonstrating that the waveform is suitable for implementation in a realizable frequency synthesis architecture of a practical radar system. The increased bandwidth of the compound waveform analyzed in this work is within the performance limits of available RF integrated circuits and can be implemented in a practical radar sensor.

Another potential use of the phase code is to encrypt the transmitted signal. The PRN code could be changed on a sweep to sweep basis or upon the completion of forming a complete range Doppler map (dwell), either could be used to discourage or prevent the use of the transmitted signal by a third party.

The compound waveform discussed here has some similarities with the class of nonlinear waveforms. The behavior of the compound waveform suggests that it may be considered to represent a special case of nonlinear modulation. However, designing a PCLFM via analysis of the individual component modulation ambiguity functions represents a familiar means to designing a PCLFM waveform.

Future research interest include examining the effects of different PRN phase codes with linear frequency modulation. Other types of bi-phase codes are also of interest, which include minimum peak sidelobe codes (MPS) and maximal length sequences. Polyphase codes such as Frank, P1 and P2 codes are also candidates for future investigation. Additionally, the behavior of the waveform in a pulsed system and evaluation of its performance in clutter and multipath environments are important areas of future work. The use of the compound PCLFM waveform in areas such as TR-MUSIC, SAR and polarimetric radar are potential application of the waveform in future efforts.

REFERENCES

1. Reneau, J. and R. Adhami, "Phase-coded LFMCW waveform analysis for short range measurement applications," *IEEE Aerospace Conference*, 1–6, Big Sky, MT, 2014.
2. Levanon, N., "CW alternatives to the coherent pulse," *IEEE Transactions on Aerospace and Electronics Ystems*, Vol. 29, No. 1, 250–254, 1993.
3. Skolnik, M., *Radar Handbook*, McGraw-Hill, New York, NY, 2008.
4. Rubio-Cidre, G., A. Badolato, L. Úbeda-Medina, B. M.-O. J. Grajal, and B. P. Dorta-Naranjo, "DDS-based signal-generation architecture comparison for an imaging radar at 300 GHz," *IEEE Transactions on Instrumentation and Measurement*, Vol. 64, No. 11, 3085–3098, November 2015.
5. Raghavendra, C. G., K. N. Bhat, M. P. R. Srivastsa, R. N. Murthy, P. V. Nayak, and N. N. S. S. R. K. Prasad, "A novel approach to generate OFDM radar signals," *International Conference on Electrical, Electronics, Communication, Computer and Optimization Techniques (ICEECCOT)*, 141–145, 2016.
6. Levanon, N., "Multifrequency complementary phase-coded radar signal," *IEEE Proceedings on Radar, Sonar and Navigation*, Vol. 147, No. 6, 276–284, 2000.
7. Ellinger, J., Z. Zhang, M. W. Wu, and Zhiqiang, "Dual-use multi-carrier waveform for radar detection and communication," *IEEE Transactions on Aerospace and Electronic Systems*, Vol. 54, No. 3, 1265–1278, 2017.
8. Y. Fu, Y. Li, Q. Huang, and K. Zhang, "Design and analysis of LFM/Barker RF stealth signal waveform," *2016 IEEE 11th Conference on Industrial Electronics and Applications (ICIEA)*, 591–595, 2016.
9. Kumar, K. R. and P. R. Kumar, "Reducing the grating lobes and main lobe width for increasing range resolution using phase and frequency modulated codes," *International Conference on Electrical, Electronics, and Optimization Techniques (ICEEOT) — 2016*, 1453–1457, 2016.
10. Xiong, G., X.-N. Yang, and H.-C. Zhao, "Pseudo-random code phase modulation and LFM combined pulse trains ranging system," *6th International Conference on ITS Telecommunication Proceedings*, 148–151, 2006.

11. Ngwar, M. and J. Wright, "Phase-coded-linear-frequency-modulated waveform for low cost marine radar system," *2010 IEEE Radar Conference*, 1144–1149, Washington D.C., 2010.
12. Seleym, A., "Complementary phase coded LFM waveform for SAR," *Integrated Communications Navigation and Surveillance (ICNS) Conference*, 4C3-1–4C3-5, 2016.
13. Zong, Z., J. Hu, and L. Zhu, "OPCDM-LFM waveform design for formation flying satellite radar system," *IEEE CIE International Conference on Radar*, 592–595, October 24–27, 2011.
14. Fu, J., G. Weim and Q. Huang, "Barker coded excitation using LFM carrier for improving axial resolution in ultrasound imaging," *Proceedings of 2013 ICME International Conference on Complex Medical Engineering*, Beijing, China, 2013.
15. Richards, M. A., J. A. Scheer, and W. A. Holm, *Principles of Modern Radar*, SciTech Publishing Inc., Raleigh, 2010.
16. Kumari, P., R. W. Heath, and S. A. Vorobyov, "Virtual pulse design for IEEE 802.11AD-based joint communication-radar," *IEEE International Conference on Acoustics, Speech and Signal Processing (ICASSP)*, 3315–3319, Calgary, 2018.
17. Fioranelli, F., S. Salous, and X. Raimundo, "Frequency-modulated interrupted continuous wave as wall removal technique in through-the-wall imaging," *IEEE Transactions on Geoscience and Remote Sensing*, Vol. 52, No. 10, 6272–6283, 2014.
18. Khomchuk, P., I. Stainvas, and I. Bilik, "Pedestrian motion direction estimation using simulated automotive MIMO radar," *IEEE Transactions on Aerospace and Electronic Systems*, Vol. 52, No. 3, 1132–1145, 2016.
19. Levanon, N. and B. Getz, "Comparison between linear FM and phase-coded CW radars," *IEE Proceedings — Radar, Sonar and Navigation*, Vol. 141, No. 4, 230–240, August 1994.
20. Rihaczek, A. W. and R. M. Golden, "Range sidelobe suppression for barker codes," *IEEE Transactions on Aerospace and Electronic Systems*, Vols. AES-7, No. 6, 1087–1092, 1971.
21. Ciuonzo, D., A. D. Maio, G. Foglia, and M. Piezzo, "Intrapulse radar-embedded communications via multiobjective optimization," *IEEE Transactions on Aerospace and Electronic Systems*, Vol. 51, No. 4, 2960–2974, 2015.
22. Ciuonzo, D., A. D. Maio, G. Foglia, and M. Piezzo, "Pareto-theory for enabling covert intrapulse radar-embedded communications," *IEEE Radar Conference (RadarCon)*, 0292–0297, Arlington, VA, 2015.
23. Ciuonzo, D. and P. S. Rossi, "Noncolocated time-reversal MUSIC: High-SNR distribution of null spectrum," *IEEE Signal Processing Letters*, Vol. 24, No. 4, 397–401, 2017.
24. Ciuonzo, D., V. Carotenuto, and A. D. Maio, "On multiple covariance equality testing with application to SAR change detection," *IEEE Transactions on Signal Processing*, Vol. 65, No. 19, 5078–5091, 2017.
25. Cheng, X., A. Aubry, D. Ciuonzo, A. D. Maio, and X. Wang, "Robust waveform and filter bank design of polarimetric radar," *IEEE Transactions on Aerospace and Electronic Systems*, Vol. 53, No. 1, 370–384, 2017.
26. U.S. Department of Commerce, National Telecommunication and Information Adminstration, Office of Spectrum Management, "United States frequency allocations — The radio spectrum," January 2016, [Online]. Available: https://www.ntia.doc.gov/files/ntia/publications/january_2016_spectrum_wall_chart.pdf., [Accessed January 11, 2017].
27. Pallavi, N., P. Anjaneyulu, P. B. Reddy, V. Mahendra, and R. Karthik, "Design and implementation of linear frequency modulated waveform using DDS and FPGA," *2017 International conference of Electronics, Communication and Aerospace Technology (ICECA)*, Vol. 2, 237–241, Coimbatore, India, 2017.
28. Ventura, J. F. I. and H. Russchenberg, "Improvement of the performance of FM-CW radar systems by using direct digital synthesizers: Comparison with voltage controlled oscillators," *2006 International Radar Symposium*, 1–4, Krakow Poland, 2006.

29. Skolnik, M. I., "An introduction and overview of radar," *Radar Handbook*, 1.1–1.24, M. I. Skolnik, Ed., McGraw-Hill, New York, 2008.
30. Siddiq, K., R. J. Watson, S. R. Pennock, P. Avery, R. Poulton, and B. Dakin-Norris, "Phase noise analysis in FMCW radar systems," *European Radar Conference (EuRAD)*, 501–504, Paris, 2015.
31. Tierney, J., C. Rader, and B. Gold, "A digital frequency synthesizer," *IEEE Transactions on Audio and Electroacoustics*, Vol. 19, No. 1, 48–57, 1971.
32. Vankka, J. and K. A. Halonen, *Direct Digital Synthesizers: Theory Design and Applications*, Springer-Verlag, New York, 2001.
33. Analog Devices, Inc., "Fundamentals of direct digital synthesis (DDS) (MT-085)," Analog Devices, Inc., Norwood, MA, 2009.
34. Andrews, G. V., C. T. M. Chang, J. D. Cayo, S. Sabin, W. A. White, and M. P. Harris, "Monolithic GaAs dual-channel digital chirp synthesiser chip," *Electronics Letters*, Vol. 27, No. 11, 905–906, May 23, 1991.
35. Scheiblhofer, S., S. Schuster, and A. Stelzer, "High-speed FMCW radar frequency synthesizer with DDS based linearization," *IEEE Microwave and Wireless Components Letters*, Vol. 17, No. 5, 397–399, May 2007.
36. Budge, M. and S. German, *Basic Radar Analysis*, Artech House, Norwood, MA, 2015.
37. Hovanessian, S. A., *Radar System Design and Analysis*, Artech House, Inc., Norwood, 1984.
38. Mahafza, B. R. and A. Z. Elsherbeni, *MATLAB Simulations for Radar Systems Design*, Chapman & Hall/CRC CRC Press LLC, Boca Raton, 2004.
39. Song, M., J. Lim, and S. Dong-Joon, "The velocity and range detection using the 2D-FFT scheme for automotive radars," *2014 4th IEEE International Conference on Network Infrastructure and Digital Content*, 507–510, Beijing, 2014.
40. Eugin, H. and J. Lee, "Hardware architecture design and implementation for FMCW radar signal processing algorithm," *Proceedings of the 2014 Conference on Design and Architectures for Signal and Image Processing*, 1–6, Madrid, 2014.
41. Swerling, P., "Probability of detection for fluctuating targets," *IRE Transactions Information Theory*, Vol. 6, No. 2, 269–308, 1960.